symmetry

MDPI

Article

Energy Dissipation Enhanced by Multiple Hinges in Bridge Piers with CFST Y-Shaped Fuses

Qunfeng Liu [1,2,*], Zhaoyang Guo [1], Xing Wu [3], Kaile Lu [1], Xiang Ren [1] and Jialong Xiao [1]

1 School of Architecture and Civil Engineering, Xi'an University of Science and Technology, Xi'an 710054, China
2 State Key Laboratory for Strength and Vibration of Mechanical Structures, School of Aerospace Engineering, Xi'an Jiaotong University, Xi'an 710049, China
3 CCCC First Highway Consultants Co., Ltd., Xi'an 710068, China
* Correspondence: qunfengliu@xjtu.edu.cn

Abstract: Concrete-filled steel tubular Y-shaped (CFST-Y) piers are good candidates for meeting the structural and aesthetic requirements of bridges. By using the theoretical and nonlinear static (pushover) analyses, the seismic performances of three types of CFST-Y piers were evaluated at different seismic hazard levels. The theoretical formulas were first proposed to estimate the lateral stiffnesses for piers with different pier–deck connections. Then, the structural ductility with the development of plastic hinges in piers was investigated based on the pushover analyses. The results demonstrate that the structural dimensions, deck mass, shear limit, and stiffness of bearings can remarkably affect the formation of hinges and thereby lead to different energy dissipation patterns to achieve the expected performance in piers. The findings suggest an economic design strategy of piers, using CFST-Y members as energy dissipation fuses with multiple hinges, to achieve low-level seismic performance cost-effectively.

Keywords: seismic design; pushover analysis; CFST; Y-shaped pier; energy dissipation

Citation: Liu, Q.; Guo, Z.; Wu, X.; Lu, K.; Ren, X.; Xiao, J. Energy Dissipation Enhanced by Multiple Hinges in Bridge Piers with CFST Y-Shaped Fuses. *Symmetry* **2022**, *14*, 2371. https://doi.org/10.3390/sym14112371

Academic Editor: Yang Yang

Received: 10 October 2022
Accepted: 7 November 2022
Published: 10 November 2022

1. Introduction

To achieve aesthetic, functional, and economic objectives simultaneously, urban bridges are usually designed to be flexible with a distinctive profile, light deck, and slender piers [1]. Recently, the Y-shaped piers have attracted the interest of architects and engineers due to their impressive appearance, small base requirement, and better transverse resistance than the one-pillar pier. Yet, under either vertical eccentric or lateral earthquake loads, the bending moments around the wye approach joint become asymmetrical. This may be detrimental to the load-bearing capacity and seismic performance of the bridge and thus, it requires much larger strength capacity and ductility in the structural members of Y-shaped piers, especially when they are used in seismic zones.

To date, performance-based seismic design has been widely accepted in civil engineering [2,3]. The design aims to achieve the desired seismic performance in structures before the consideration of their strength requirements, which demands enhanced ductility and strength in structural members simultaneously. It was reported that the confined concrete under transverse reinforcement had contributed a lot to the post-yielding ductility and strength in reinforced concrete (RC) and concrete-filled steel tubular (CFST) members [4–6]. Chacón et al. [7] characterized the good flexural ductility of CFST piers with a large allowable lateral displacement. Many experiments [8,9] have also demonstrated the highly efficient energy dissipation in CFST columns. Therefore, to obtain better seismic performance, CFST members have remarkable advantages in strength and ductility at the same structural dimensions [10,11].

Particularly, when the Y-shaped piers are designed to meet the aesthetic requirement, CFST members become preferred candidates to meet the performance demand and strength demand with the nearly minimal member cross-section. With the slender members, the

CFST Y-shaped (CFST-Y) piers may possess low ductility demand due to the global slenderness, leading to redundant ductility in some localized members. This redundant ductility capacity has also been reported in earthquake-damaged CFST columns [12] to obtain further fire resistance. In addition, the residual seismic performance, characterized as enhanced ductility and energy dissipation before failure, was observed in the RC columns retrofitted with fiber composite wraps [13]. Albeit, the well-known ductility redundancy in CFSTs, the residual ductility capacity [14] beyond seismic demand was still not exploited.

To address the seismic challenges in structures on account of functionalities and site conditions, the capacity design strategy was proposed by deliberately designing some 'ductile' members at a relatively lower capacity to protect the 'brittle' members in the structural system [15,16]. Based on this strategy, some structural members with redundant ductility can be designed to act as fuses that help the overall structure meet the global ductility demand on achieving the desired seismic performance [17–19]. To achieve different performance objectives at the corresponding seismic hazard levels, a practical design of fuses was proposed by Yang et al. [20] with the equivalent energy design procedure. This energy-based procedure facilitates the seismic analyses of structures with the consideration of the residual ductility of CFST members.

At present, seismic analyses of structures were usually conducted through the pushover method by graphically comparing the structural response under the given earthquake event with the target performance at a specific hazard level [21–23]. Using this method, some researchers have evaluated the seismic performances of bridges at the corresponding shaking intensities [24,25]. However, previous works were mainly focused on the seismic evaluation of the typical highway or railway piers where additional dampers were used for energy dissipation [26,27]. There are scarce reports on the seismic evaluation of pier systems by utilizing CFST members for extra energy dissipation.

The goal of this work is to propose an enhanced energy dissipation strategy for piers with CFST Y-shaped fuses. To obtain this goal, the effects of the design parameters in piers, bearings, decks, and pier–deck connections will be investigated on the formation of multiple hinges that determined the progressive energy dissipations before and after the expected performance. The study will try to seek an approach for enhancing energy dissipation in piers by exploiting the CFST Y-shaped members.

2. Models and Methods

2.1. CFST-Y Bridge Pier Models

In three types of Y-shaped piers considered in this work, as shown in Figure 1, both the lower columns and the upper limbs are built of circular CFST members with identical diameters of 0.6 m for the limbs and 1.0 m for the column. The total pier heights (h) range from 4 m to 10 m, which is comprised of the column height (h_2) and the limb height (h_1) varying from 1 m to 7 m individually. The center-to-center spacings (d) between two limb tops range from 1.2 m to 7.2 m. All CFST members are made of Q345 steel tubes with a thickness of 16 mm forming a Y-shaped pier filled with C35 concrete [28]. The bottom end of the column is assumed to be rigidly connected to the foundation cap fixed at ground level and the soil–structure interaction is neglected for simplicity.

In typical multi-span continuous bridges, piers are usually connected to the superstructures with rigid connections monolithically or the bearings elastically. In bearing-supported bridges, the Y-shaped piers can be further divided into two categories: one with a steel tension bracing installed between the two limb tops and the other without bracing. To denote the structural configuration, we named the three types of pier systems by their pier–deck connections: the monolithic piers, the braced articulated piers, and the free articulated piers.

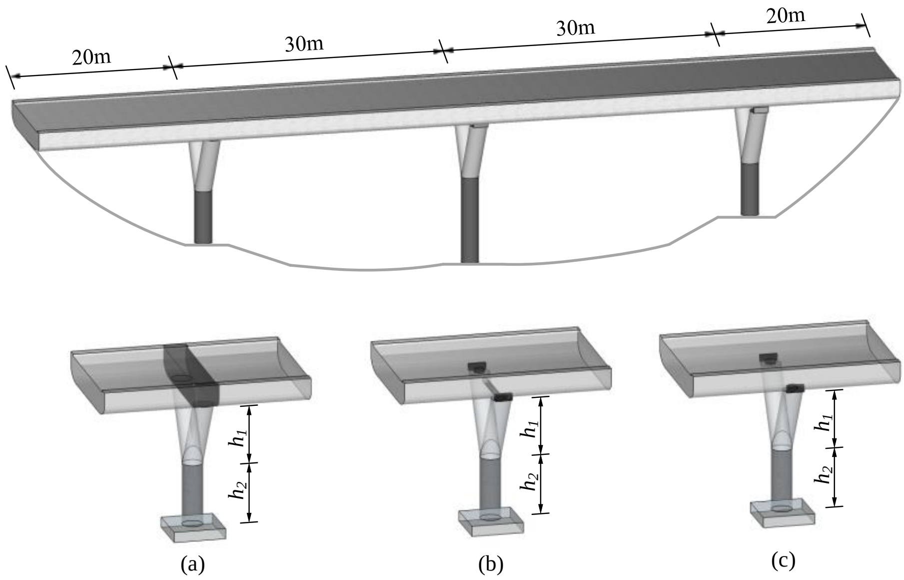

Figure 1. Sketches and typical pier models for three types of bridges with the monolithic piers (**a**), the braced articulated piers (**b**), and the free articulated piers (**c**), respectively.

2.2. Pushover Methodology

The seismic design of bridges was usually conducted by nonlinear static (pushover) analysis [29]. This analysis is prevailing in the conceptual seismic design due to its simplicity, easy explanation, and low cost [30]. In this work, inelastic static analyses are conducted to study the seismic performances of the CFST-Y piers. With large lateral resistance, this Y-shaped pier is often used in urban bridges to support decks at similar low to modest heights. In pushover analysis, the pier–deck system can be considered as an equivalent single-degree-of-freedom (SDF) model. When a horizontal force is applied to the deck mass, the pier is assumed to deform in the first vibration mode. According to the displacement-based design approach [31], the deck displacement can be limited within an accepted range by designing the initial stiffness and yielding strength of the pier. Thus, a conceptual design can be conducted by evaluating the deformation and yielding behaviors of the pier under pushover loading.

For seismic evaluation of the Y-shaped piers, we performed static inelastic (pushover) analyses based on the recommended procedures in ATC 40 [32] to estimate the strength and deformation demands under Design-Based Earthquakes (DBE). First, non-linear pushover analyses [30] are performed to deform the equivalent SDF model in the first mode shape with the P-delta effect considered. The relationship between the shear forces and their corresponding displacements is plotted as the capacity curve. Then, the capacity curve is transformed into the Acceleration Displacement Response Spectrum (ADRS) that correlates spectral acceleration (S_a) with spectral displacement (S_d) [19,33].

According to the Chinese seismic code [28], the elastic response spectra under design earthquakes can be selected according to the assumption of damping ratio (usually 5%) and site conditions. The design spectra can thus be transformed into the acceleration spectra for girder bridges under Service-Level Earthquakes (SLEs), as shown in Figure 2. However, as the seismic hazard level increases to the Maximum Credible Earthquake (MCE) level, structures will yield under earthquakes, and the original damping ratio will be modified accordingly. To capture the post-yielding performance in CFST-Y piers, the inelastic design spectrum for each pier system was derived from its elastic design spectrum with the modified equivalent damping and then converted into the target performance demand spectrum [34]. Thereafter, a performance point for each pier can be obtained by intersecting its capacity spectrum with the inelastic response spectrum at a given earthquake level.

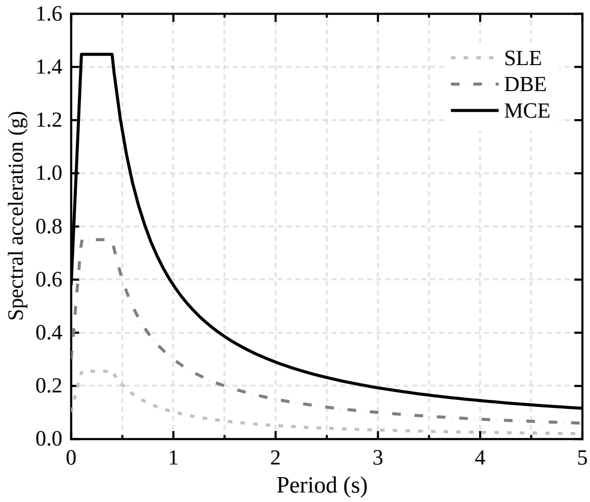

Figure 2. Acceleration spectra for piers at different hazard levels.

2.3. Numerical Models

Simplified bridge models with three types of CFST-Y piers are built by using an open-source nonlinear finite-element analysis software OpenSees (v3.2.2, UC Berkeley, Berkeley, CA, USA) from the Pacific Earthquake Engineering Research Center [35], as shown in Figure 1a–c, respectively. The numerical models in this study were verified by using another commercial software called Midas/Civil [36]. In each model, the pier is simulated with fiber-based beam elements, whose typical cross-section is comprised of an outer thin-walled steel tube and confined concrete, as shown in Figure 3. The steel tubes are modeled with 12 outer-layer fibers with bilinear strain-hardening behavior at the elastic modulus (E_s) of Q345 steel in the first linear stage, and 0.01 E_s in the post-yielding stage. The confined concrete is divided into 48 fibers described by the Kent–Park model [37,38], which performs well in modeling both the concentrated and the distributed plastic hinges in CFSTs [6].

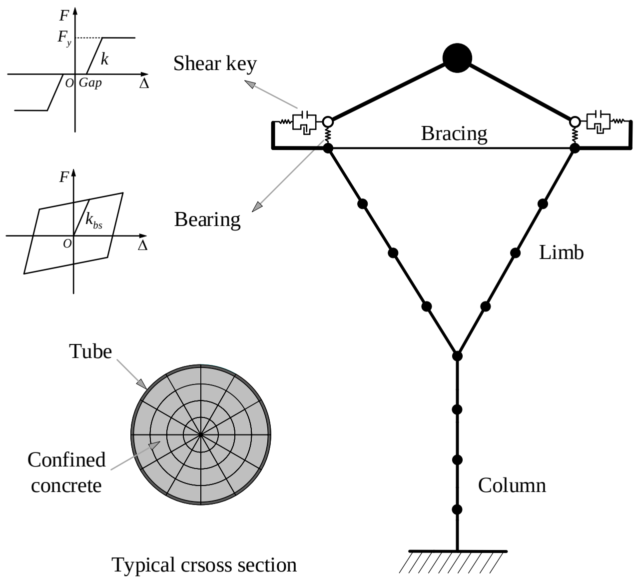

Figure 3. SDF finite element models for the braced articulated pier systems with a typical fibred column cross-section.

Piers connect to the deck by rigid links directly in monolithic bridges. While in bearing-supported bridges, piers connect to the deck through both rigid links and rubber bearings in series. In these cases, bearings are modeled with bilinear beam elements. A standard type of rubber pad bearings [39], with shear stiffness k_b at 4370 kN/m, serve as elastic links to support the deck. Two equivalent tributary masses for the pier systems are considered in this work, depending on the corresponding span length and deck material.

To prevent catastrophes under severe earthquakes, shear keys are usually installed to protect the bridge from unexpected failures. In both articulated piers, the shear limit of the bearings is assumed to be either 5 cm or 10 cm by nearly rigid restrainers. The shear limit can be modeled with a combined gap, composed of a compression gap and a tension gap in parallel, and then in series connected with an elastic spring with much larger elasticity, i.e., 5 times the shear elasticity of bearings. The shear keys are installed between each limb and the deck, preventing the deck from sliding when the shear deformations of bearings exceed the predefined shear limit. This detailing design is a necessary provision required by the seismic design codes in China [40] which can also ensure the ductility of CFST members exploited before the yielding of bearings.

3. Results and Discussion

3.1. Lateral Stiffnesses for Three Types of Y-Shaped Piers

Figure 4 shows the simplified diagrams of three types of Y-shaped piers made of CFST members. In each diagram, a wye approach pier consists of two inclined limbs (with identical height h_1 and top spacing d) and one vertical pier column (with height h_2). In the two connected limbs, the equivalent moment of inertia of each limb is I_1 and the inclined angle between the two limbs is 2α. The lower column, with the equivalent moment of inertia at I_2, connects the two upper limbs rigidly with a casting wye joint.

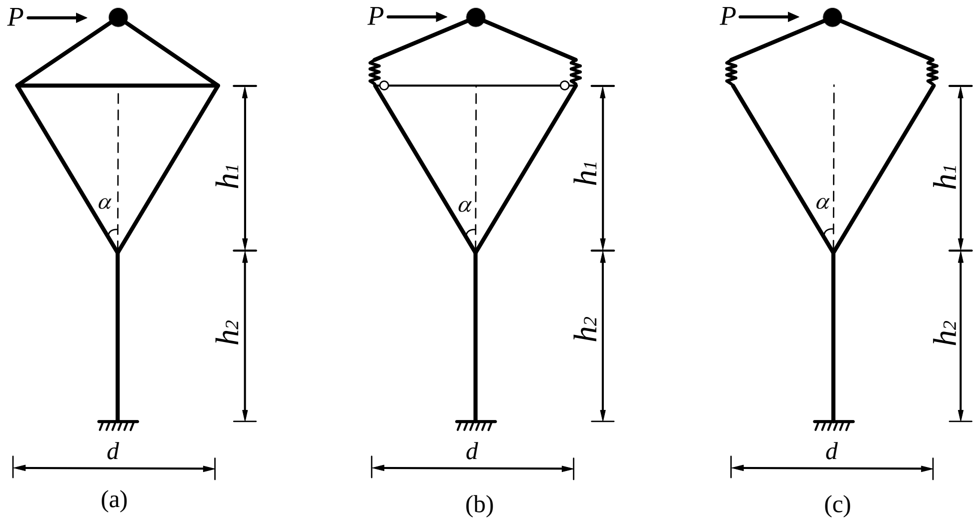

Figure 4. Simplified diagrams for CFST-Y pier systems with the monolithic (**a**) and the articulated pier–deck connections with (**b**) or without bracing (**c**).

In this work, the piers systems are categorized by their pier–deck connections: the monolithic, the braced articulated, and the free articulated piers. For simplification, the shear deformation of CFST members is ignored. Thus, under the equivalent lateral static loading (P) on the bridge deck (with the effective mass of m), the lateral stiffnesses of the three equivalent SDF pier systems can be calculated by the following Equations (1), (3), and (6), respectively.

$$k_{p1} = \left(\frac{1}{k_{c1}} + \frac{1}{k_{c2}} \right)^{-1} \tag{1}$$

where $k_{c1} = \frac{6EI_1}{h_1^3 \cos\alpha}$ is the lateral stiffness of the two limbs in the pier, and E is the equivalent elastic modulus for the CFSTs. The lateral stiffness of the column can be expressed as:

$$k_{c2} = \left(\frac{h_1 h_2^2}{2EI_2} + \frac{h_2^3}{3EI_2} + \frac{{h_1}^2 h_2}{EI_2} + \frac{h_1 h_2^2}{3EI_2}\right)^{-1} = \frac{3EI_2}{h_2^3}\left(1 + 2.5\frac{h_1}{h_2} + 3\left(\frac{h_1}{h_2}\right)^2\right)^{-1} \quad (2)$$

The lateral stiffness of the articulated piers with bracing can be expressed as:

$$k_{p2} = \left(\frac{1}{2k_{bs}} + \frac{1}{k_{l1} + k_{l2}} + \frac{1}{k_{c2}}\right)^{-1} \quad (3)$$

Where tension deformation in bracing is assumed to be negligible, k_{bs} is the shear stiffness of a single bearing, and the lateral stiffnesses of the left and right limbs can be calculated by Equations (4) and (5), respectively.

$$k_{l1} = \frac{3EI_1 \cos\alpha}{h_1^2(h_1 - d/2\lambda)} \quad (4)$$

$$k_{l2} = \frac{3EI_1 \cos\alpha}{h_1^2(h_1 + d/2\lambda)} \quad (5)$$

where λ is the ratio of the lateral seismic force to the equivalent gravity of deck (P/mg). The lateral stiffness of the free articulated piers can be expressed as:

$$k_{p3} = \left[\frac{1}{k_{e1} + k_{e2}} + \frac{1}{k_{c2}}\right]^{-1} \quad (6)$$

where $k_{e1} = \frac{k_{l1}k_{bs}}{k_{l1}+k_{bs}}$ and $k_{e2} = \frac{k_{l2}k_{bs}}{k_{l2}+k_{bs}}$ are the equivalent lateral stiffnesses of the two inclined limb-bearing systems that support the deck together.

All the above equations depend on their structural dimensions (h_1, h_2, and d) and the material properties, like E, I_1, and I_2. It indicates that piers with different pier–deck connections have distinct equations of lateral stiffnesses.

Three groups of piers are modeled at the constant circular cross-sections (d_1 = 0.6 m, d_2 = 1.0 m) but with different structural dimensions (h_1, h_2, and d). The lateral stiffnesses (k_{p1}, k_{p2}, and k_{p3}) of the monolithic, the braced articulated and the free articulated piers are calculated and listed in Table 1, respectively. For each case with identical structural dimensions, k_{p1} is generally larger than k_{p2} and k_{p3}. As h increases from 4 m to 10 m with the increase of either h_1 or h_2 individually, all lateral stiffnesses (k_{p1}, k_{p2}, and k_{p3}) decrease monotonically. The stiffness reduction as a function of h is much more significant for k_{p1} than for k_{p2} and k_{p3}, indicating that the monolithic piers are more sensitive to pier height. The stiffness reduction due to the increase of h_1 is larger than that due to h_2. It is noted that the influence of inter-limb spacing d on the lateral stiffnesses of the monolithic piers is not so significant as that of h_1 and h_2.

Table 1. Lateral stiffnesses and ductility capacities for three groups of piers with varying structural dimensions.

h (m)	h_1 (m)	h_2 (m)	d (m)	k_{p1} (10^3 kN/m)	Δ_{u1} (cm)	k_{p2} (10^3 kN/m)	Δ_{u2} (cm)	k_{p3} (10^3 kN/m)	Δ_{u3} (cm)
4	**1**	3	3.6	93.09	9.01	7.97	8.15	7.71	8.41
6	**3**	3	3.6	20.83	15.01	6.91	14.71	5.90	14.01
8	**5**	3	3.6	7.05	29.51	4.88	29.51	4.39	27.81
10	**7**	3	3.6	3.11	31.01	3.48	30.61	2.66	30.22
4	3	**1**	3.6	39.40	6.65	8.19	6.81	6.81	6.81
6	3	**3**	3.6	20.83	15.01	6.91	14.71	5.90	14.01
8	3	**5**	3.6	10.87	19.01	5.30	19.45	4.68	18.01
10	3	**7**	3.6	6.06	24.71	3.82	24.21	3.49	23.55

Table 1. *Cont.*

h (m)	h_1 (m)	h_2 (m)	d (m)	k_{p1} (10^3 kN/m)	Δ_{u1} (cm)	k_{p2} (10^3 kN/m)	Δ_{u2} (cm)	k_{p3} (10^3 kN/m)	Δ_{u3} (cm)
6	3	3	**1.2**	21.95	14.51	6.97	14.41	6.18	13.85
6	3	3	**3.6**	20.83	15.01	6.91	14.71	5.90	14.01
6	3	3	**6.0**	19.16	15.11	6.84	15.31	4.91	15.21
6	3	3	**7.2**	18.29	16.31	6.80	15.81	4.58	15.51

3.2. Ductility Capacities for Piers with Different Pier–Deck Connections

The seismic evaluation of each pier is carried out by comparing the structural capacity with the desired performance demand at a certain seismic hazard level. To identify the yielding state of the pier, the initial yielding of the outmost layer fibers is termed the first yielding, and the full development of the plastic hinge is termed the second yielding. The ductility capacity of each pier can be characterized by the post-yielding displacement capacity [41], Δ_u, defined by the difference between the ultimate deck displacement, u_u, to the corresponding displacement, u_y, at its second yielding.

$$\Delta_u = u_u - u_y \tag{7}$$

The ductility demand, Δ_0, of each pier is determined by the difference between the displacement demand at a given earthquake level and the corresponding displacement at the second yielding.

$$\Delta_0 = u_0 - u_y \tag{8}$$

Similarly, the ductility capacities (Δ_{u1}, Δ_{u2}, and Δ_{u3}) of the three types of piers, as listed in Table 1, are calculated with Equation (7) based on u_u and u_y obtained from their corresponding capacity spectra. For cases listed in Table 1, the ductility capacity and the corresponding ductility demands at three earthquake levels (SLE, DBE, and MCE) are compared by bar charts, as illustrated in Figure 5. Generally, Δ_{u1}, Δ_{u2}, and Δ_{u3} are comparable to each other with the fixed structural dimensions. For each case with h increasing from 4 m to 10 m, all ductility capacities (Δ_{u1}, Δ_{u2}, and Δ_{u3}) increase monotonically with the increase of either h_1 or h_2 individually. Yet, as d increases from 1.2 m to 7.2 m, ductility capacities for three types of piers (h_1 = h_2 = 3 m) do not change significantly, as shown in Figure 5c,f,i. This implies that the pier height, comprising h_1 and h_2, is the primary parameter that influences structural ductility.

For all cases, piers deform elastically with a negative Δ_0 less than $-0.25\ u_y$ at the first yielding, elastic-plastically with a negative Δ_0 larger than $-0.25\ u_y$, and plastically with positive Δ_0. Under the SLE loading, the ductility demand for each case is less than $-0.25\ u_y$. This means that all piers remain elastic upon the SLE demands being reached and the requirement on the immediate occupancy (IO) performance level being achieved. Similar IO performances can be achieved in both the monolithic piers and the braced articulated piers under the DBE loading. Yet, for the free articulated piers, the ductility demands (Δ_0) exceed the corresponding $-0.25\ u_y$ and even become positive for piers with heights of 6 m and 8 m. This means that the free articulated piers will deform inelastically to meet the DBE demands that should be checked against the requirements of the life safety (LS) performance. For all considered piers, the ductility demands (Δ_0) at the MCE level are positive, meaning that all piers yield with the formation of plastic hinges to achieve the collapse prevention (CP) performance.

Besides, the yielding behaviors of each pier under the MCE earthquake are illustrated in the upper region of each diagram in Figure 5. The first yielding regions are colored in green and the second yielding regions (hinges) are in red. It is noticed that most free articulated piers yield at the DBE and the MCE levels with multiple hinges forming sequentially, the first at the bottom ends of their upper limbs and the second at the bottom end of their columns. This provides an alternative way to dissipate more energies with multiple hinges by selecting the free articulated pier–deck connection.

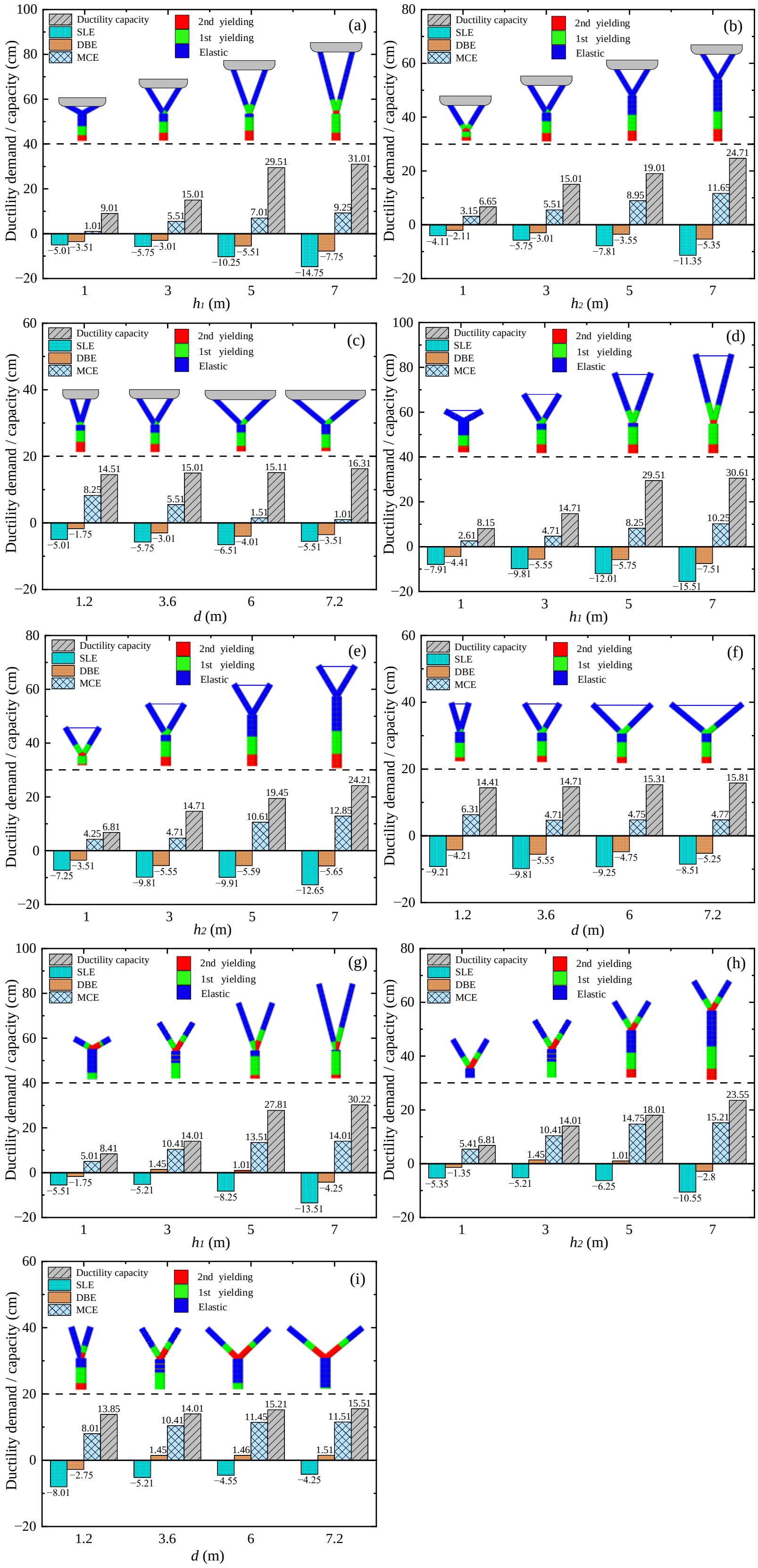

Figure 5. Ductility demands, ductility capacities, and yielding behaviors for piers with the monolithic connection (**a**–**c**), the articulated connections with (**d**–**f**) and without bracing (**g**–**i**) at varying structural dimensions.

3.3. Ductility Capacities and Lateral Resistances for Piers with Different Structural Dimensions

Figures 6–8 present the acceleration displacement response spectra (ADRSs) and the corresponding capacity spectrum curves for the monolithic piers, the braced articulated piers, and the free articulated piers, respectively. With the increase of either h_1 or h_2, the lateral resistance decreases, while the ductility capacity increases. In each figure, capacity spectrum curves intersect with their inelastic MCE response spectra at the MCE performance points, denoted as solid circles.

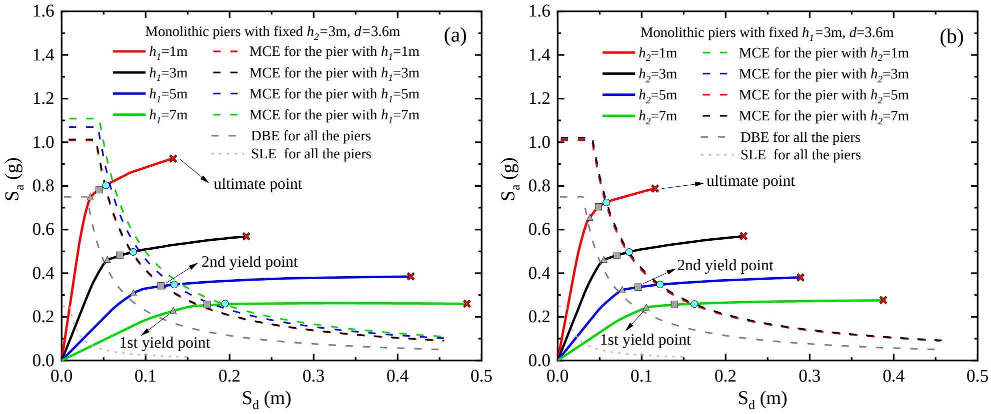

Figure 6. ADSRs for the monolithic piers at different limb heights (**a**) and column heights (**b**).

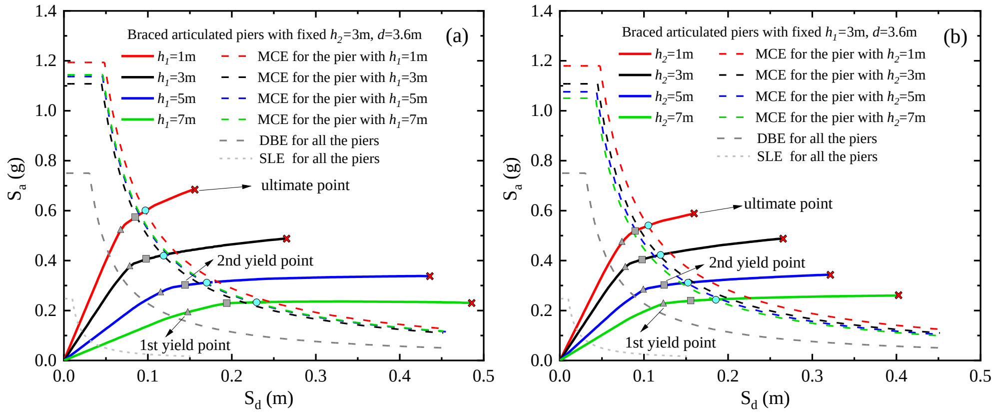

Figure 7. ADSRs for the braced articulated piers at different limb heights (**a**) and column heights (**b**).

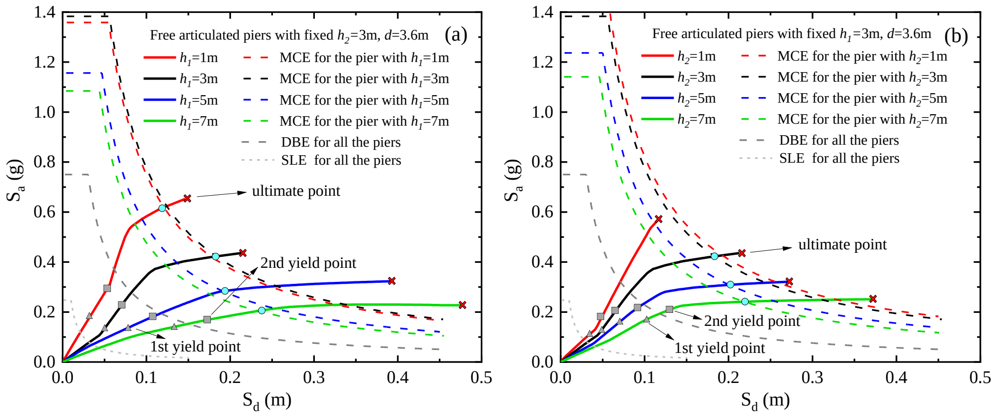

Figure 8. ADSRs for the free articulated piers at different limb heights (**a**) and column heights (**b**).

The first yielding point, the second yielding point, and the ultimate failure point for each pier are marked as the triangle, the cube, and the cross, respectively. From the markers shown in Figures 6–8, we can conclude that, for each pier considered, its MCE performance point is always located between its second yielding point and its ultimate failure point, while its SLE performance point is located below its first yielding point. This confirms the yielding behaviors illustrated in Figure 5 where all piers deform elastically to achieve the IO performance and yield with the formation of hinges to achieve the CP performance.

In the monolithic and the braced articulated piers, both yielding points locate between the corresponding DBE and the MCE performance points; while in the free articulated piers, both yielding points locate between the SLE and the DBE performance points except the highest pier (h = 10 m). In the free articulated piers, the lateral stiffness of limbs (k_{l1} or k_{l2}) is rather small relative to the shear keys and column. Under lateral loading, the horizontal displacement at the pier top is distributed according to the slenderness of the structural members. The limb inclined towards the displacement direction is usually the slenderest member and will yield earlier; but at increased h, the slenderer pier can accommodate more deformation and will yield later. This indicates that, besides the pier–deck connection, the yielding behaviors are affected by the distribution of lateral stiffnesses among the bearings and the structural members.

3.4. Ductility Demands at Different Deck Masses, Shear Limits, and Stiffnesses of Bearings

Figure 9 represents the ADRS curves for three types of piers with identical structural dimensions ($h_1 = h_2 = 3$ m, d = 3.6 m). Two practical equivalent deck masses (1.0×10^5 kg and 1.5×10^5 kg) are considered to study the lateral resistance and the ductility of the interested piers. With either deck mass, the lateral resistance of the monolithic pier is larger than that of the braced articulated pier, and further, the free articulated one; whereas the ductility capacity for the three types of piers is in the opposite order.

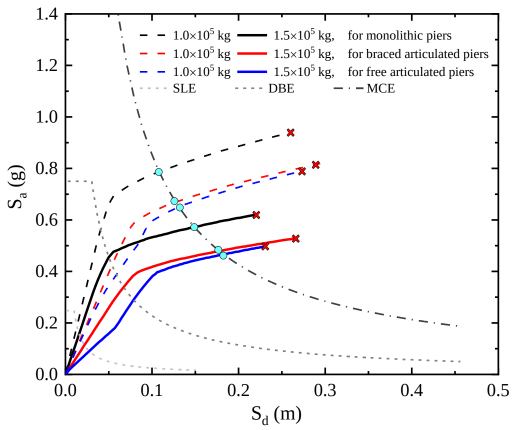

Figure 9. ADRS curves for three types of piers with different deck masses.

It is noted that piers with large masses have decreased strength capacity and increased deformation capacity. This indicates that heavy bridges demand a large deformation capacity, whereas light bridges demand a large strength capacity. Thus, in light pedestrian bridges, like the Streicker Bridge [42] on the Princeton University campus, the monolithic pier is preferred for its large resistance; but in heavy bridges, articulated piers are recommended for the large deformation capacity in bearings. A better energy absorption capacity introduced by bearings was also demonstrated by Abey et al. [43] in bearing-supported bridges.

In articulated bridges, shear keys are usually installed to limit the shear deformation of bearings. At the fixed structural dimensions ($h_1 = h_2 = 3$ m, d = 3.6 m), the ADRS curves for the pushover analyses in the braced and free articulated piers with bearings at different stiffnesses and shear limits are shown in Figures 10 and 11, respectively. Three stiffnesses ($0.5k_b$, k_b, and $2k_b$) and two shear limits (5 cm and 10 cm) are considered for each type of articulated piers.

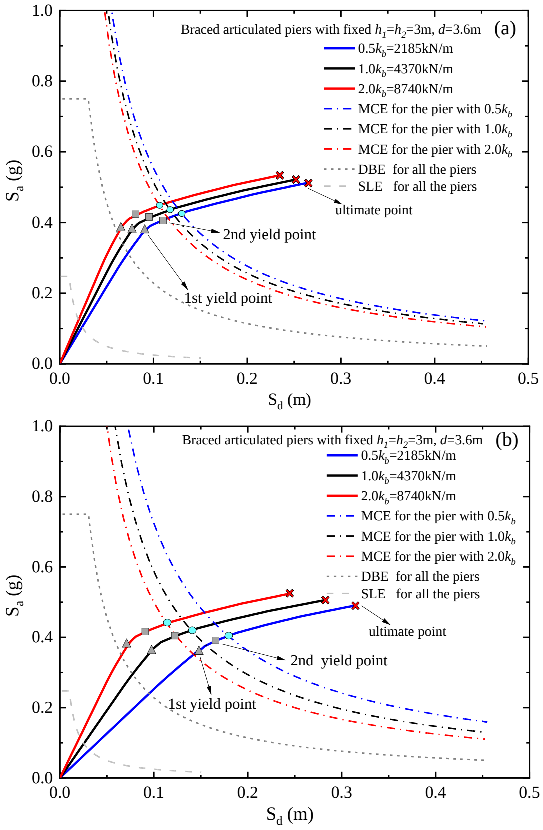

Figure 10. ADRSs for pushover analyses in braced articulated piers with bearing shear limits of 5 cm (**a**) and 10 cm (**b**).

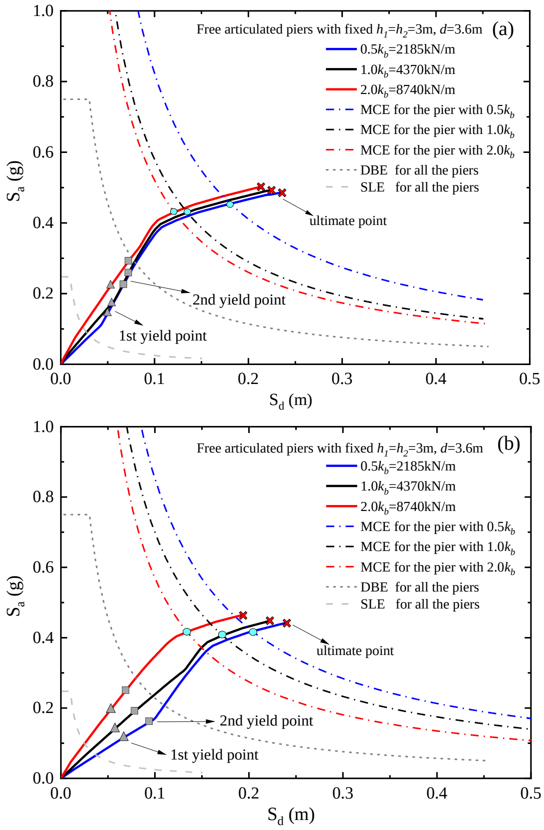

Figure 11. ADRSs for pushover analyses in free articulated piers with bearing shear limits of 5 cm (**a**) and 10 cm (**b**).

For both articulated piers, the ductility demands increase as the shear stiffnesses decrease from $2k_b$ to $0.5k_b$, as typically shown in Figure 10. For braced articulated piers, both the first and the second yielding points are located between the DBE and MCE performance points; while for each free articulated pier, both yielding points are between the SLE and DBE performance points. This indicates that both articulated piers deform elastically to satisfy their corresponding SLE performance demands, but the free articulated piers will form plastic hinges before the DBE performance demands. Particularly, for the free articulated piers with $0.5k_b$, as shown in Figure 11b, a transition occurs before the DBE demand. The early yielding confirms the illustrations in Figure 5g–c, where limbs yield before columns.

As the shear limit increases from 5 cm to 10 cm, the ductility demands increase significantly while the strength demands decrease slightly to achieve MCE performance, as illustrated in 10b and 11b. This demonstrates that the ductility demand of the articulated Y-shaped piers can be remarkably enhanced by inserting a larger gap between the bearing and the shear keys.

3.5. Energy Dissipation before and after the Expected Performance

Figure 12 presents three distinct hysteretic curves for three types of CFST-Y piers with identical structural dimensions at h of 6 m under cyclic loading. The curves before and after the MCE performance are colored in blue and black, respectively. For the monolithic pier as illustrated in Figure 12a, the ultimate horizontal load is ~1005 kN. The absorbed energy before the MCE performance is 226.2 kN·m, and after the MCE performance, the residual energy to be dissipated before failure is 293.0 kN·m. This indicates that the monolithic pier has balanced energy dissipations before and after the MCE performance. For the braced articulated pier as illustrated in Figure 12b, the maximum horizontal load is ~1545 kN. The absorbed energy before the MCE performance is 115.0 kN·m, the least among the three; while the residual energy before failure is 376.2 kN·m, the largest among the three. This indicates that the braced articulated pier has the least energy dissipation before the MCE performance. For the free articulated pier as illustrated in Figure 12c, the maximum horizontal load is ~1575 kN. The energy absorbed before the MCE performance is 344.0 kN·m, the largest among the three; while the residual energy before failure is 162.6 kN·m, the smallest among the three. This indicates that the free articulated pier has the largest energy dissipation before the MCE performance.

The absorbed energy before the desired performance can be characterized as the post-yielding ductility between the first yielding and the corresponding performance point. This determines to what extent the local ductility of structural members can be utilized for mitigating the intended earthquake shakings. On the other side, the residual energy before failure can be characterized as the redundant ductility between the performance point and the ultimate ductility capacity. The larger redundant ductility the pier has, the more safety redundancy it remains. Thus, in the seismic design of CFST Y-shaped piers, a proper pier–deck connection should be first selected to decide the energy dissipation strategy before and after the desired performance.

Figure 13 shows the absorbed and residual energies, corresponding to the respective upper and bottom contour diagrams, for the three types of piers with different structural dimensions. For each type of pier, both energies are functions of the two structural dimensions (h_1 and h_2), both ranging from 1 m to 7 m. Consistent with the case ($h_1 = h_2 = 3$ m) shown in Figure 12, the energy dissipations of each type of pier differ remarkably before and after the MCE performance and are determined by the structural dimensions. That is, with the identical cross-sections in the CFST-Y piers, the structural dimensions determine the stiffness of structural members and thereby, the absorbed and residual energies.

For the high piers with small global stiffnesses, both the absorbed and residual energies are small regardless of the pier–deck connections, as shown in the top-right corner of each diagram; except, the absorbed energies of the braced articulated piers are usually less than that of the monolithic piers, and further less than that of free articulated piers; whereas the residual energies of the braced articulated piers are usually larger than that of the monolithic piers, and further larger than that of free articulated piers. The opposite orders in the absorbed and residual energy dissipation suggested that the braced articulated piers are preferred if the largest safety redundancy is pursued. However, if cost-effectiveness is pursued, the free articulated piers are preferred for achieving a specific performance under low-level earthquakes. In this case, the inclined members in the free articulated pier may act as fuses for extra energy dissipation.

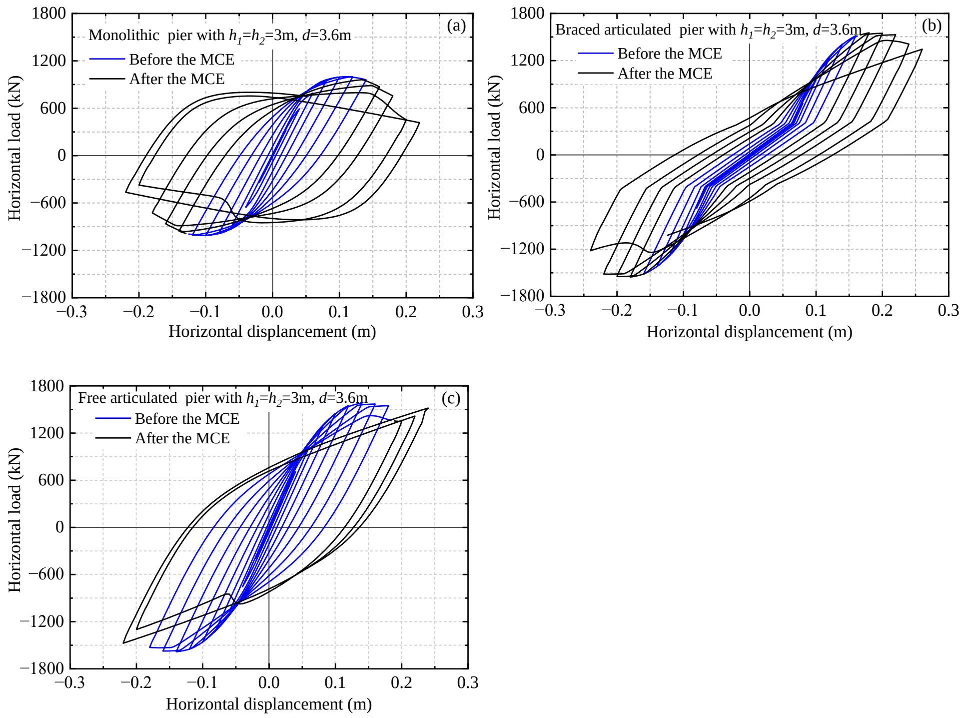

Figure 12. Hysteretic curves for the monolithic (**a**), the braced articulated (**b**), and the free articulated (**c**) CFST-Y piers with h_1 = h_2 = 3 m and d = 3.6 m.

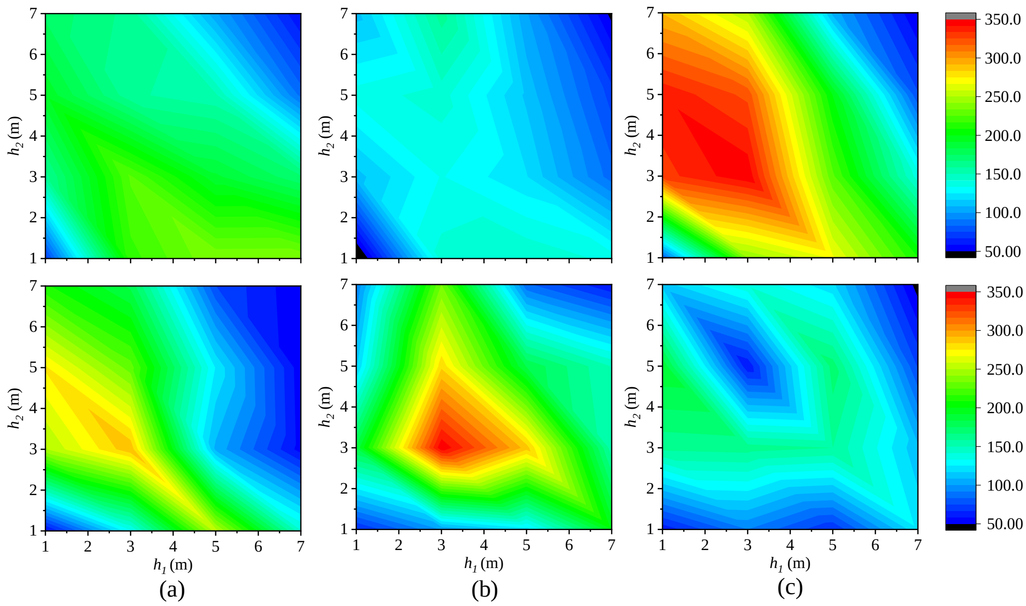

Figure 13. Contour diagrams of the absorbed energy (upper) and the residual energy (bottom) in achieving the MCE performance for the monolithic (**a**), the braced articulated (**b**), and the free articulated piers (**c**) with different structural dimensions.

Figure 14 shows the skeleton curves obtained from the hysteretic curves of the free articulated piers. The effects of the three structural dimensions such as h_1, h_2, and d on the horizontal load and displacement can be studied individually based on Figure 14a–c, respectively. With the increase of either h_1 or h_2, the ultimate strength of the skeleton curves decreases, while the ultimate displacement increase. This means that the less ultimate strength, always accompanied by the larger ultimate displacement, is determined by h. It is also noted that both the lateral resistance and the ductility capacity are nearly insensitive to d. This confirms that the nonsymmetrical moment near the wye approach joint is insensitive to d and solely determined by the combined stiffnesses (k_{e1} or k_{e2}) of limb-bearing systems. Here, at the fixed shear limit of 5 cm, the structural ductility of the free articulated pier is primarily determined by the combination of h_1 and h_2. Thus, by rationally designing the structural dimensions (h_1 and h_2), the local ductility of inclined members can be exploited to dissipate more energy effectively.

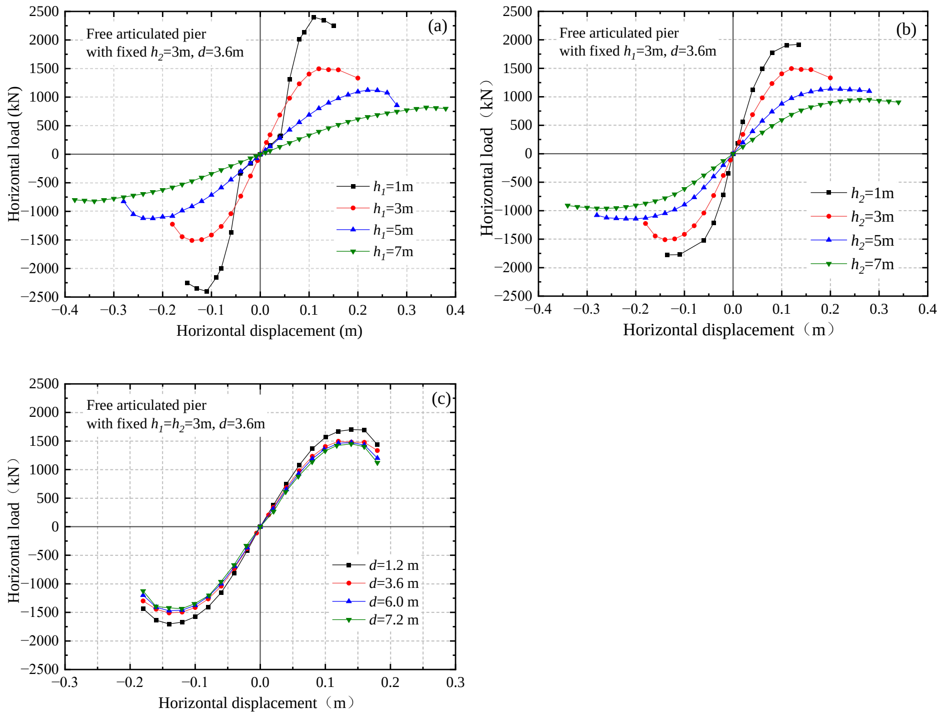

Figure 14. Skeleton curves in the free articulated piers at different h_1 (**a**), h_2 (**b**), and d (**c**).

4. Conclusions

This work proposed an energy-based approach for enhancing the seismic performance of the CFST-Y bridge piers. The effects of the structural dimensions, masses, shear limits, and bearing stiffnesses on the ductility capacity and ductility demands were studied for pier systems with different pier–deck connections. By comparing the ductility capacity with the ductility demand, performance objectives (IO, SL, and CP) at different seismic hazard levels can be achieved with different energy dissipation patterns in piers. Some conclusions can be drawn as follows:

(1) The pier–deck connection and structural dimensions (h_1, h_2, and d) determine the lateral stiffnesses and yielding behaviors of the CFST Y-shaped piers that will further influence the lateral resistances and ductility capacities in bridges at the SLE, DBE, and MCE hazard levels.

(2) On achieving the expected performance objectives, the ductility demands for all three types of piers increase with the deck mass. Particularly, for the braced and free articulated piers, the ductility demands increase with the shear limit but decrease with the shear stiffness of bearings.

(3) The absorbed and residual energies before and after the expected performance can be utilized to evaluate the ductility exploitation and performance redundancy in CFST-Y piers. The enhanced absorbed energies before the MCE performance were observed in the free articulated piers where the extra energies were dissipated by multiple hinges formed in CFST Y-shaped fuses.

This work provided a conceptual approach to evaluate the seismic performance of the CFST-Y bridge piers. According to the energy dissipation patterns in three types of piers, an enhanced energy dissipation mechanism by multiple hinges was proposed in the free articulated piers where the local ductility of the CFST Y-shaped members can be efficiently exploited by appropriately selecting pier–deck connections and primary design parameters. However, the findings obtained in this study are based on a pedestrian case bridge with small deck masses and fixed cross-sections in pier–deck systems. In practice, more detailed designs on the structural dimensions should be considered for achieving the expected performance objectives and multiple hinges. Nonetheless, this approach provides insight into the energy dissipation enhancement in bridge piers via the CFST Y-shaped fuses for economic consideration. In the future, studies can be conducted on applying the CFST Y-shaped fuses to bridges with large deck masses or structures to be retrofitted for obtaining a compromise between cost-effectiveness and safety redundancy.

Author Contributions: Q.L.: Conceptualization, writing—review and editing, funding acquisition; Z.G.: Investigation, writing—original draft preparation; X.W.: Writing—review and editing, project administration; K.L.: Software, data curation; X.R.: Writing—review and editing, validation; J.X.: Data curation. All authors have read and agreed to the published version of the manuscript.

Funding: This research was funded by the National Natural Science Fund Committee of China (Grant No. 11632014, 51808444), Scientific Research Program of Shanxi Provincial Education Department (18JK0502), State Key Laboratory for Strength and Vibration of Mechanical Structure open Foundation (Grant No. SV2018-KF-35), Startup Foundation of XUST (Grant No. 2018YQ2-05).

Institutional Review Board Statement: Not applicable.

Informed Consent Statement: Not applicable.

Data Availability Statement: The models and some data of the three typical bridge piers (the monolithic pier, the braced articulated pier, and the free articulated pier) used in this study are available in the repository of GitHub via https://github.com/zhaoyang-guo/opensees.git (accessed on 31 October 2022).

Conflicts of Interest: The authors declare no conflict of interest.

Nomenclature

CFST	concrete-filled steel tubular
RC	reinforced concrete
CFST-Y	CFST Y-shaped
SDF	single-degree-of-freedom
S_a	spectral acceleration
S_d	spectral displacement
ADRS	Acceleration Displacement Response Spectrum
SLE	Service Level Earthquake
DBE	Design Based Earthquake
MCE	Maximum Credible Earthquake
IO	Immediate Occupancy
LS	Life Safety
CP	Collapse Prevention
h	total pier height
h_1	limb height
h_2	column height

d	center-to-center spacing between the limb tops
E_s	elastic modulus of Q345 steel
α	inclined angle between one limb and the vertical line
I_1	moment of inertia of limb
I_2	moment of inertia of column
P	equivalent lateral static loading
m	effective mass of bridge deck
k_{p1}	lateral stiffness of the monolithic piers
k_{p2}	lateral stiffness of the braced articulated piers
k_{p3}	lateral stiffness of the free articulated piers
k_{c1}	lateral stiffness of the upper portion of the Y-shaped pier
k_{c2}	lateral stiffness of the lower portion of the Y-shaped pier
E	equivalent elastic modulus of CFSTs
k_b	shear stiffness of bearings in a pier system
k_{bs}	shear stiffness of a single bearing
k_{l1}	lateral stiffness of the left limb
k_{l2}	lateral stiffness of the right limb
λ	ratio of the lateral seismic force to the equivalent gravity of deck
k_{e1}	equivalent lateral stiffness of the left limb-bearing systems
k_{e2}	equivalent lateral stiffness of the left limb-bearing systems
Δ_u	post-yielding displacement capacity
Δ_0	ductility demand
u_u	ultimate deck displacement
u_y	the second yielding displacement
u_0	displacement demand at a given earthquake level
Δ_{u1}	ductility capacity of the monolithic pier
Δ_{u2}	ductility capacity of the braced articulated pier
Δ_{u3}	ductility capacity of the free articulated pier

References

1. Yang, S.; Huang, D. Aesthetic considerations for urban pedestrian bridge design. *J. Archit. Eng.* **1997**, *3*, 3–8. [CrossRef]
2. Priestley, M. Performance based seismic design. *Bull. N. Z. Soc. Earthq.* **2000**, *33*, 325–346. [CrossRef]
3. Priestley, M.J.N.; Calvi, G.M.; Kowalsky, M.J. Direct displacement-based seismic design of structures. In Proceedings of the NZSEE Conference, Wellington, New Zealand, 30 March–1 April 2007; pp. 1–23.
4. D'Amato, M.; Braga, F.; Gigliotti, R.; Kunnath, S.; Laterza, M. A numerical general-purpose confinement model for non-linear analysis of R/C members. *Comput. Struct.* **2012**, *102–103*, 64–75. [CrossRef]
5. Guney, O.; Saatcioglu, M. Confinement of concrete columns for seismic loading. *Struct. J.* **1987**, *84*, 308–315.
6. Stephens, M.T.; Lehman, D.E.; Roeder, C.W. Seismic performance modeling of concrete-filled steel tube bridges: Tools and case study. *Eng. Struct.* **2018**, *165*, 88–105. [CrossRef]
7. Chacon, R.; Mirambell, E.; Real, E. Strength and ductility of concrete-filled tubular piers of integral bridges. *Eng. Struct.* **2013**, *46*, 234–246. [CrossRef]
8. Elremaily, A.; Azizinamini, A. Behavior and strength of circular concrete-filled tube columns. *J. Constr. Steel. Res.* **2002**, *58*, 1567–1591. [CrossRef]
9. Marson, J.; Bruneau, M. Cyclic testing of concrete-filled circular steel bridge piers having encased fixed-based detail. *J. Bridge Eng.* **2004**, *9*, 14–23. [CrossRef]
10. Han, L.-H.; Li, W.; Bjorhovde, R. Developments and advanced applications of concrete-filled steel tubular (CFST) structures: Members. *J. Constr. Steel. Res.* **2014**, *100*, 211–228. [CrossRef]
11. Roeder, C.W.; Stephens, M.T.; Lehman, D.E. Concrete filled steel tubes for bridge pier and foundation construction. *Int. J. Steel Struct.* **2018**, *18*, 39–49. [CrossRef]
12. Wang, J.; Kunnath, S.; He, J.; Xiao, Y. Post-Earthquake Fire Resistance of Circular Concrete Filled Steel Tubular Columns. *J. Struct. Eng.* **2020**, *146*, 1–13. [CrossRef]
13. Chung, Y.-S.; Park, C.K.; Meyer, C. Residual seismic performance of reinforced concrete bridge piers after moderate earthquakes. *ACI. Struct. J.* **2008**, *105*, 87–95.
14. Bertero, R.D.; Bertero, V.V. Redundancy in earthquake-resistant design. *J. Struct. Eng.* **1999**, *125*, 81–88. [CrossRef]
15. Paulay, T.; Priestley, M. *Seismic Design of Reinforced Concrete and Masonry Buildings*; John Wiley & Sons, Inc.: Hoboken, NJ, USA, 1992; pp. 95–157.
16. Bovo, M.; Savoia, M.; Praticò, L. Seismic Performance Assessment of a Multistorey Building Designed with an Alternative Capacity Design Approach. *Adv. Civ. Eng.* **2021**, *2021*, 5178065. [CrossRef]

17. Zhang, C.; Tian, Y. Simplified performance-based optimal seismic design of reinforced concrete frame buildings. *Eng. Struct.* **2019**, *185*, 15–25. [CrossRef]
18. Kia, S.M.; Yahyai, M. Relationship between local and global ductility demand in steel moment resisting frames. In Proceedings of the World Conference on Earthquake Engineering WCEE, Vancouver, BC, Canada, 1–6 August 2004.
19. Fajfar, P. Capacity spectrum method based on inelastic demand spectra. *Earthq. Eng. Struct. D* **1999**, *28*, 979–993. [CrossRef]
20. Yang, T.Y.; Tung, D.P.; Li, Y. Equivalent energy design procedure for earthquake resilient fused structures. *Earthq. Spectra.* **2018**, *34*, 795–815. [CrossRef]
21. Zou, X.K.; Chan, C.M. Optimal seismic performance-based design of reinforced concret-e buildings using nonlinear pushover analysis. *Eng. Struct.* **2005**, *27*, 1289–1302. [CrossRef]
22. Ghobarah, A. Performance-based design in earthquake engineering: State of development. *Eng. Struct.* **2001**, *23*, 878–884. [CrossRef]
23. Cardone, D.; Dolce, M.; Palermo, G. Direct displacement-based design of seismically isolated bridges. *Bull. Earthq. Eng.* **2009**, *7*, 391–410. [CrossRef]
24. Guo, W.; Hu, Y.; Liu, H.; Bu, D. Seismic performance evaluation of typical piers of China's high-speed railway bridge line using pushover analysis. *Math. Probl. Eng.* **2019**, *2019*, 95147691. [CrossRef]
25. Wang, P.-H.; Chang, K.-C.; Dzeng, D.-C.; Lin, T.-K.; Hung, H.-H.; Cheng, W.-C. Seismic evaluation of reinforced concrete bridges using capacity-based inelastic displacement spectra. *Earthq. Eng. Struct. Dyn.* **2021**, *50*, 1845–1863. [CrossRef]
26. Sadeghi, M.A.; Yang, T.Y.; Bagatini-Cachuço, F.; Pan, S. Seismic design and performance evaluation of controlled rocking dual-fused bridge system. *Eng. Struct.* **2020**, *212*, 110467. [CrossRef]
27. Liu, Q.F.; Zhu, S.M.; Yu, W.S.; Wu, X.; Song, F.; Ren, X. Ground Motion Frequency Insensit-ivity of Bearing Supported Pedestrian Bridge with Viscous Dampers. *KSCE. J. Civ. Eng.* **2021**, *25*, 2662–2673. [CrossRef]
28. *JTG/T 2231-01-2020*; Specifications for Seismic Design of Highway Bridges. Chongqing Communications Research Institute: Chongqing, China; People's Communication Publishing: Beijing, China, 2020.
29. FEMA. *NEHRP Guidelines for the Seismic Rehabilitation of Buildings*; FEMA-273; Applied Technology Council for the Building Seismic Safety Council: Washington, DC, USA, 1997.
30. Krawinkler, H.; Seneviratna, G. Pros and cons of a pushover analysis of seismic performance evaluation. *Eng. Struct.* **1998**, *20*, 452–464. [CrossRef]
31. Calvi, G.M.; Pavese, A. Conceptual design of isolation systems for bridge structures. *J. Earthq. Eng.* **1997**, *1*, 193–218. [CrossRef]
32. *ATC-40*; Seismic Evaluation and Retrofit of Concrete Buildings. Applied Technology Council: Redwood City, CA, USA, 1996.
33. Fajfar, P. A nonlinear analysis method for performance-based seismic design. *Earthq. Spectra.* **2000**, *16*, 573–592. [CrossRef]
34. Lagaros, N.D.; Fragiadakis, M. Evaluation of ASCE-41, ATC-40 and N_2 static pushover methods based on optimally designed buildings. *Soil. Dyn. Earthq. Eng.* **2011**, *31*, 77–90. [CrossRef]
35. McKenna, F. Open System for Earthquake Engineering Simulation. OpenSees. Available online: https://opensees.berkeley.edu/ (accessed on 3 July 2020).
36. Midas/Civil. *Nonlinear FE Software for Bridge Design & Analysis*; Midas Information Technology Co., Ltd.: Seongnam, Korea, 2000.
37. Scott, B.D.; Park, R.; Priestley, M.J.N. Stress-Strain Behavior of Concrete Confined by Overlapping Hoops at Low and High Strain Rates. *J. Proc.* **1982**, *79*, 13–27.
38. Susantha, K.; Ge, H.; Usami, T. Uniaxial stress-strain relationship of concrete confined by various shaped steel tubes. *Eng. Struct.* **2001**, *23*, 1331–1347. [CrossRef]
39. *JTJ 663-2006*; Series of Elastomeric Pad Bearings for Highway Bridges. CCCC Highway Consultants Co., Ltd. People's Communications Publishing: Beijing, China, 2007.
40. *GB50011-2010*; Code for Seismic Design of Buildings. China Ministry of Construction. China Architecture & Building Press: Beijing, China, 2010.
41. Fan, L.C.; Zhuo, W.D. *Ductility Seismic Design of Bridges*; People's Communication Publishing: Beijing, China, 2001.
42. Sigurdardottir, D.H.; Glisic, B. *Measures of Structural Art: A Case Study Using Streicker Bridge*; Princeton University: Princeton, NJ, USA, 2013; pp. 275–284.
43. Abey, E.T.; Somasundaran, T.P.; Sajith, A.S. Significance of elastomeric bearing on seismic response reduction in bridges. In *Advances in Structural Engineering*; Springer: New Delhi, India, 2015; pp. 1339–1352.